An apparatus for qualitative assessment of the shading ratio of oblique illumination and real-time high-contrast imaging

Received: 21 April 2022 | Revised: 30 July 2022 | Accepted: 5 August 2022

DOI: 10.1002/jbio.202200122

RESEARCH ARTICLE

JOURNAL OF BIOPHOTONICS

An apparatus for qualitative assessment of the shading ratio of oblique illumination and real-time high-contrast imaging

Meng Shao[1,2] | **Ke Wang**[3] | **Zixin Wang**[1] | **Tao Peng**[1] | **Shuhe Zhang**[4] | **Juanlin Zhang**[1] | **Shu Fang**[1] | **Fengsong Wang**[3] | **Shengzhao Zhang**[1] | **Min-Cheng Zhong**[2] | **Yi Wang**[1] | **Zhensheng Zhong**[1] | **Jinhua Zhou**[1,5]

[1]School of Biomedical Engineering, Anhui Medical University, Hefei, Anhui, China

[2]School of Instrument Science and Opto-Electronic Engineering, Hefei University of Technology, Hefei, Anhui, China

[3]School of Life Science, Anhui Medical University, Hefei, Anhui, China

[4]University Eye Clinic Maastricht, Maastricht University Medical Center, Maastricht, The Netherlands

[5]Anhui Provincial Institute of Translational Medicine, Anhui Medical University, Hefei, Anhui, China

Correspondence
Jinhua Zhou, School of Biomedical Engineering, Anhui Medical University, Hefei, Anhui 230032, China.
Email: zhoujinhua@ahmu.edu.cn

Funding information
Natural Science Foundation of Anhui Province in China, Grant/Award Number: 1908085MA14; Research Fund of Anhui Institute of Translational Medicine, Grant/Award Number: 2021zhyx-B16

Abstract

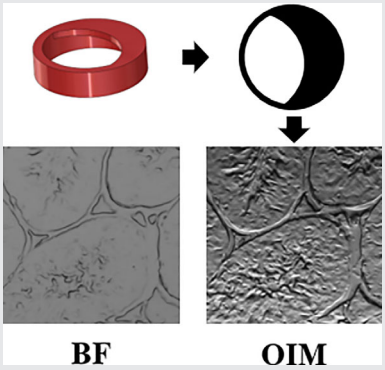

Oblique illumination imaging can significantly improve the contrast of transparent thin samples. However, in traditional oblique illumination methods, either the condenser is offset or a block is added to the condenser, which makes it complicated and challenged to build a stable oblique illumination imaging. Herein, we present a method to measure the optimal shading ratio of oblique illumination in an inverted microscope, and develop an apparatus for stable high-speed high-contrast imaging with uniform brightness. At optimal shading ratio, the oblique illumination imaging has better imaging quality than differential interference contrast, which characteristic is independent on sample. In oblique illumination with low magnification objective, the images have uneven brightness. According to target brightness, we have developed a brightness unevenness correction algorithm to form uniform background brightness for oblique illumination. Integrating the algorithm with imaging acquisition, corrected oblique illumination microscopy is appropriate to observe living cells with high contrast.

KEYWORDS

brightness correction, high contrast, image quality assessment, oblique illumination, shading ratio

1 | INTRODUCTION

As a tool for observing the microscopic world, optical microscope plays a very important role in different disciplines and provides detailed visualization data for scientific researches [1]. Among many microscopic imaging techniques, bright field (BF) is still the most common one. However, for unlabeled cells and thin tissues, the contrast of BF microscopy images is relatively low. In order to improve the contrast of imaging, many new microscopic imaging techniques have been developed, including dark field, phase contrast (PC) [2, 3], differential interference contrast (DIC) [4] and modulation contrast [5]. All these techniques involve modulating the illuminating beam, generally by adding prisms, polarizers, or phase plates

to the condenser system. Then filtered or modulated at the image plane of the objective. As a result, in these methods the optical elements are expensive, and the optical path structure is so precise that it is difficult to implement [6, 7].

Oblique illumination microscopy (OIM) is another technique to improve the contrast of images. The past few decades have witnessed enormous growth in the development [8–11] and applications [12–15] of this technology in a wide variety of disciplines. For conventional oblique illumination techniques [16–19], only part of the illuminating light rays deviating from the optical axis is allowed to pass through the condenser of a microscopy system. Due to its simple structure, OIM can be easily modified by a BF microscope to improve image contrast. Therefore, this microscopy has features of low cost and high contrast, that can be used in different samples such as diatoms [20] and live buccal epithelial cells [21]. Traditional oblique illumination imaging methods improve the contrast of transparent objects by offsetting condensers or blocking parts of imaging lighting [22]. However, in these methods, the oblique illumination shading ratio and the position of the shades are adjusted based on subjective visual feedback, which is not stable. The invariant shading aperture model can be used to form oblique illumination which can improve the imaging stability. Previous studies on the design of shading aperture model show that meniscus shape is a better choice [20]. Nevertheless, the shading ratio of this model has not been studied in detail. Moreover, to the best of our knowledge, no method has been reported to measure the best shading ratio for oblique illumination in real microscopes.

In this article, we construct an apparatus for the first time to assess the optimal shading ratio of the oblique illumination. For the Olympus IX73 microscope, an adjustable illuminating aperture diaphragm is designed and installed on the condenser. The stepping motor drives the sliding diaphragm to gradually increase the shading ratio and the image is collected at the same time. Then, the corresponding shading ratio is obtained when the image contrast is the best through the image quality assessment (IQA) function. Under the optimal shading ratio, we demonstrated that our microscope can stably improve imaging contrast for different samples by oblique illumination. In spite of the uneven brightness appears on the image in this situation, which is most obvious under low magnification, we realized real-time correction of image brightness by implying a brightness correction algorithm. In our investigations, quantitative OIM can achieve high-contrast imaging of living cells by means of appropriate shading ratio.

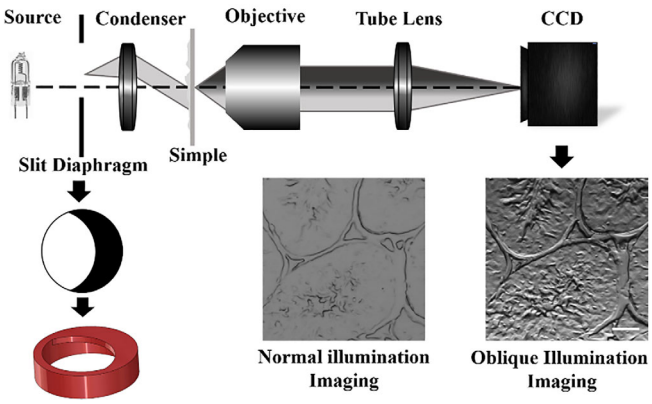

FIGURE 1 Schematic of the oblique illumination microscopy. Scale bar, 50 μm

2 | MATERIALS AND METHODS

2.1 | Oblique illumination microscopy

In this article, the oblique illumination imaging is implemented on a commercial microscope (Olympus, IX73, Japan). Figure 1 depicts a schematic of the OIM. In the light path of Köhler illumination, an asymmetric slit diaphragm is added above the condenser to partly block illumination light. Then the light rays obliquely transmit through a sample and are collected by an objective. Those rays from the sample are imaged in a camera via a tube lens. A three-dimensional model of the specific diaphragm and the real object printed with polylactic acid material by 3D printer are shown in the insert below light path of microscope. In subsequent applications, the diaphragm is fixed on the condenser. Under oblique illumination, the microscopic image of a mouse testis tissues is shown in the inset below the camera of charged coupled device (CCD) (MindVision, MV-SUA231GM-T, China).

2.2 | Quantitative oblique illumination for microscopic imaging

To assess this oblique illumination imaging, the shading ratio should be gradually changed. A assemble slit diaphragm module is driven by a motor, as shown in Figure 2. In Figure 2A, a stepping motor (Shanghai Lianyi, XM60H-20-1G, China) is fixed on a lifting platform. For the components of assembly, as shown in Figure 2B, the fixed diaphragm (blue) is installed on the condenser of the inverted microscope while the sliding diaphragm (red) is installed on the plate extended from the motor. The fixed diaphragm and the sliding diaphragm have the same size (radius is 49.5 mm) as the aperture of the condenser. In the 3D model, the sliding diaphragm driven by stepping motor

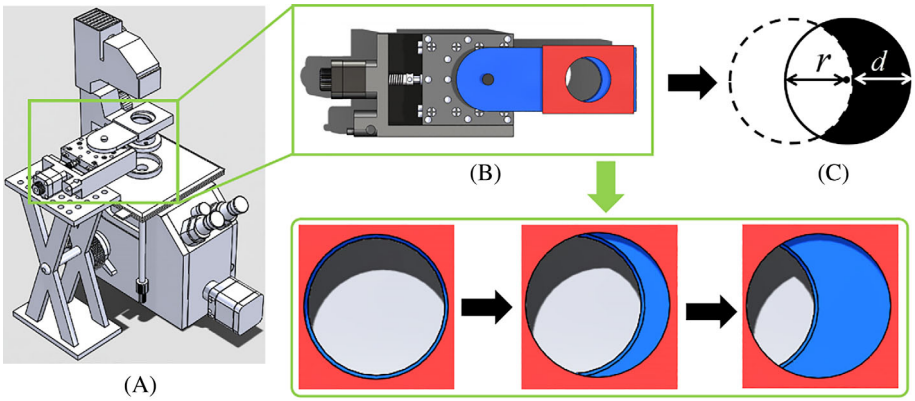

FIGURE 2 Quantitative method of oblique illumination. (A) The schematic experimental device. (B) Stepping motor changing slit diaphragm, and the illustration depicts shading ratio being gradually increased. (C) A simplified model for calculating shading ratio

can move relative to the fixed diaphragm. All of them are fabricated with 3D printing. When the sliding diaphragm moves along x direction with a distance of d, the light rays passing through the slit diaphragm will be partly blocked due to confluence of two apertures, as shown in Figure 2C. If the sliding diaphragm and fixed diaphragm have same radius of r, shading area S_b for blocking rays has the relationship of

$$S_b = 2 \times \left(\int_{-\frac{d}{2}}^{r} \sqrt{r^2 - x^2}\,dx - \int_{-\frac{d}{2}}^{r-d} \sqrt{r^2 - (x+d)^2}\,dx \right). \quad (1)$$

This equation is derived in Section S1 in Supplementary Material.

Then the area of the illumination light passes the slit diaphragm can be expressed as

$$S_p = \pi r^2 - S_b. \quad (2)$$

Thus, the shading ratio R can be determined by

$$R = \frac{S_b}{S_p + S_b}. \quad (3)$$

When the sliding diaphragm deviates from the fixed diaphragm, R varies with sliding distance, as shown in the illustration. The oblique illuminance varies with the change of non-axial symmetric area. In this process, the stepping motor is controlled by a customized LabVIEW (National Instruments) program with movement at a step of 0.1 mm. During the movement, the images of the sample are captured by a CCD camera works for capturing and observing this process for different proportions.

2.3 | Image quality assessment

Previous studies have shown that image quality of OIM was characterized by five features: the Haralick's texture inertia [23], the local contrast [24], the variance of the Laplacian [25], the angle measure technique spectrum [26] and the anisotropic quality index [27]. In these features, the local contrast provides good assessments for the contrast, and the variance of the Laplacian can be used to measure sharpness [28]. These two methods can be used to quantitatively assess the image quality for different shading ratios of oblique illumination. Under ×10 objective, the images of HeLa cells are analyzed with previous five features. The average of the local contrast and the variance of the Laplacian is consistent with the average of previous five features for OIM images assessment (Section S2 in Supplementary Material). Thus, the IQA function can be denoted by the average of the local contrast and the variance of Laplacian.

The local contrast [24] was used to calculate the local intensity contrast of each pixel with its eight neighbors. First, the image patch is divided into 3 × 3 cells. Second, the difference between maximum and minimum values of the local range of each cell is calculated for a local range image (I_{RF}). Finally, the local contrast value LC is obtained by averaging all the pixels of I_{RF}. The local contrast value LC can be represented by

$$LC = \frac{1}{MN} \sum_{i=1}^{M} \sum_{j=1}^{N} I_{RF}(i,j), \quad (4)$$

where M and N represent the numbers of rows and columns of each image.

It is a common method to assess image sharpness using the variance of the Laplacian [25]. This assessment function can be expressed as:

$$VarLAP = \frac{1}{MN} \sum_{i=1}^{M} \sum_{j=1}^{N} \left[L(i,j) - \overline{|L|} \right]^2, \quad (5)$$

where $L(i, j)$ represents the convolution of the image and the Laplacian operator, and $\overline{|L|}$ is the mean of absolute

values of $L(i, j)$. The convolution kernel of Laplacian operator is:

$$h = \frac{1}{6}\begin{pmatrix} 0 & -1 & 0 \\ -1 & 4 & 1 \\ 0 & -1 & 0 \end{pmatrix}.$$

For high imaging quality, the observed objects in a microscopic image should have good contrast and image sharpness. In this study, the quantitative assessment of image is described as:

$$IQA = \frac{LC + VarLAP}{2}. \quad (6)$$

In our next experiments, *IQA* is used to assess OIM. For each step of the motor, *LC* and *VarLAP* of the captured image are calculated, respectively. For all images, the *LC* and *VarLAP* are normalized to 1 by means of peak value, respectively. When $IQA = 1$, the image quality is the best.

2.4 | Brightness correction

As shading ratio of the illumination increasing, the nonuniformity of brightness distribution of the image increases. To obtain uniform illumination distribution, we proposed a method for real-time correction. The correction algorithm is based on the fact that the average gray value of pixels of each row changes linearly in the image. In correction process, $aveI_i$ represents the average gray value of pixels in row i, and Var_T is the target gray value for correction. Then the correction coefficient k_i can be determined by

$$k_i = \frac{Var_T}{aveI_i}\,(i = 1, 2, 3...), \quad (7)$$

where i denotes the ith row of the image. The corrected image I_{cor} can be described as:

$$I_{cor(i,j)} = I_{(i,j)} \cdot k_i\,(i, j = 1, 2, 3...), \quad (8)$$

$I_{i,j}$ represents the intensity of a pixel at ith row and jth column.

3 | RESULTS

3.1 | Slice imaging

We observed onion epidermal cells and mouse testis tissues under different shading ratios. Under BF imaging with a ×10 objective, the sliding diaphragm was pulled by a stepping motor to gradually increase the shading ratio, then 400 images were captured with automatic exposure. The target gray value for automatic exposure is set to 120. According to Equation (6), *IQA* was calculated for each image. Figure 3A shows the normalized data of *IQA* on onion epidermal cells. When R is gradually increased from 0% to ~50%, the image quality does not obviously change. But it is evidently demonstrated that the image quality rapidly increases with R at ~55%. The image quality reaches the maximum value when R is at 66.74%, and then the image quality drops sharply. When R reaches about 70%, the image quality drops to zero. If the exposure is fixed with a specific time interval, the improvement is lower than that of automatic exposure (Section S3 in Supplementary Material). Figure 3B is the BF image ($R = 0$), and the illustrations show the red and purple regions when the R are 0%, 50%, 66.74% and 75%, respectively. At the edge of the onion cells, the imaging contrast with $R \sim 66.74\%$ is the best among the images with different shading ratios. This performance confirms the validity of *IQA* for imaging quality.

IQA of unstained mouse testis tissue in OIM is shown in Figure 3C. From the data of *IQA*, the IQA also does not obviously change when R is less than 50%. This means that there is no obvious improvement relative to BF imaging. While R is beyond ~55%, *IQA* also increases rapidly and reaches the maximum at $R = 67.80\%$. Thereafter, the image quality drops sharply too. In this case, the image quality is improved, and the texture details are also improved compared to BF imaging. When $R \sim 70\%$, *IQA* also drops to zero, and the imaging contrast decreases due to low illumination light. In Figure 3D, the two local regions (red and purple) in the image of mouse testis tissue also demonstrate that the imaging contrast at $R = 66.80\%$ is better than those of other R values including BF imaging. Comparing OIM with BF microscopy, the imaging contrast for this tissue can be enhanced by oblique illumination with an appropriate shading ratio.

For onion epidermal cells and mouse testis tissue in Figure 3, the best imaging quality has a slight difference in two cases, but the general trend of the IQA vs shading ratio is similar. When $R < 50\%$, the imaging quality in two cases is not significantly improved. For R varying from 60% to 68%, the imaging quality has considerable improvement and the texture details are obvious. Thus, microscopic image can be obviously improved by oblique illumination with a specific designed diaphragm.

3.2 | Imaging HeLa cells in a petri dish

In Figure 4, the images of HeLa cells were captured from Olympus series objectives of ×10 (NA = 0.30), ×20

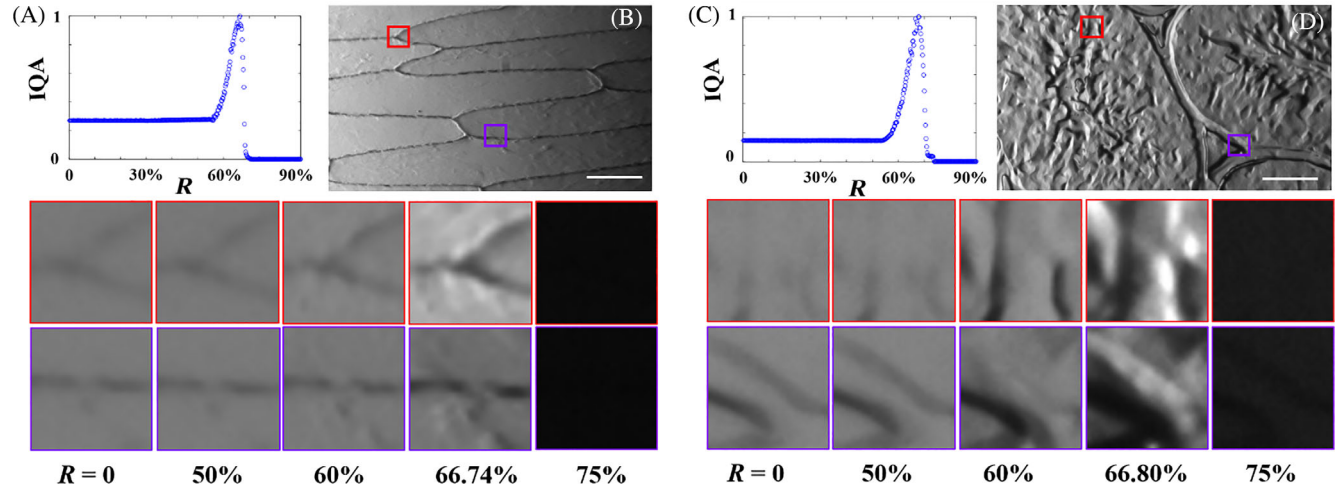

FIGURE 3 Imaging quality assessment under a ×10 objective. (A and B) Image quality assessment (IQA) curve and the image of onion cells is obtained in optimal oblique illumination scheme, respectively. (C and D) IQA curve and the image of mouse testis tissue is obtained in optimal oblique illumination scheme, respectively. Illustrations show the oblique illumination with different *R*. Scale bar, 50 μm

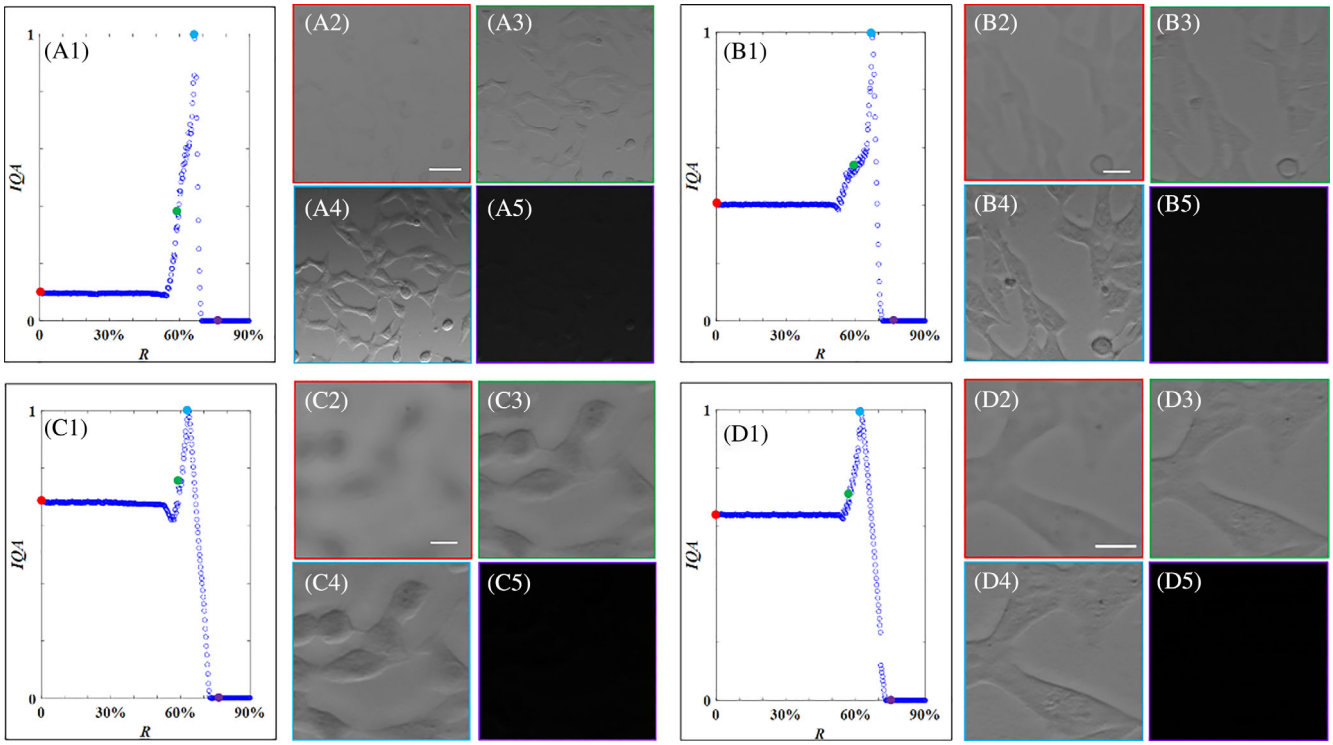

FIGURE 4 HeLa cells under ×10 (A), ×20 (B), ×40 (C) and ×60 (D) objectives. (A1-D1) Image quality assessment curve of different shading ratios. (A2-D2), (A3-D3) and (A4-D4) The images of *R* at 50%, best *R*, and 75%, respectively. Scale bars, 50 μm (A), 20 μm (B) and 10 μm (C and D)

(NA = 0.70), ×40 (NA = 0.75) and ×60 (NA = 1.00). The normalization results of *IQA* are shown in Figure 4A1-D1. As the objective magnification increasing, the trends of *IQA* vs *R* are similar, but the initial *IQA* and the best ratio for imaging quality are different. When *R* varies at the range of 0% to 50%, the *IQA* for each objective remains stable. For the four objectives, the images of HeLa cells at *R* = 50% are shown in Figure 4A2-D2. This status corresponds to the green circle in the *IQA* vs *R* curve. In these situations, the imaging contrast is similar to that of BF imaging (*R* = 0, not shown). For four objectives, the *IQA* vs *R* curves can be divided into two groups, and each group has similar trend. One is the low magnification objectives including ×10 and ×20 objectives.

TABLE 1 *IQA* of various imaging modes under different magnification objectives

Objective type	Experimental sample	Best *IQA*	Optimal shading ratio (%)	*IQA* of DIC imaging	*R* for imaging quality equivalent to DIC (%)
×10	Onion cells	0.02435	66.74	0.02062	63.31
	Mouse testis tissues	0.07689	67.80	0.04946	63.52
	HeLa cells	0.02302	67.16	0.01464	60.24
×20	HeLa cells	0.02306	66.95	-	-
×40	HeLa cells	0.02838	63.74	-	-
×60	HeLa cells	0.02625	62.87	0.02015	59.13

Abbreviations: DIC, differential interference contrast; IQA, image quality assessment.

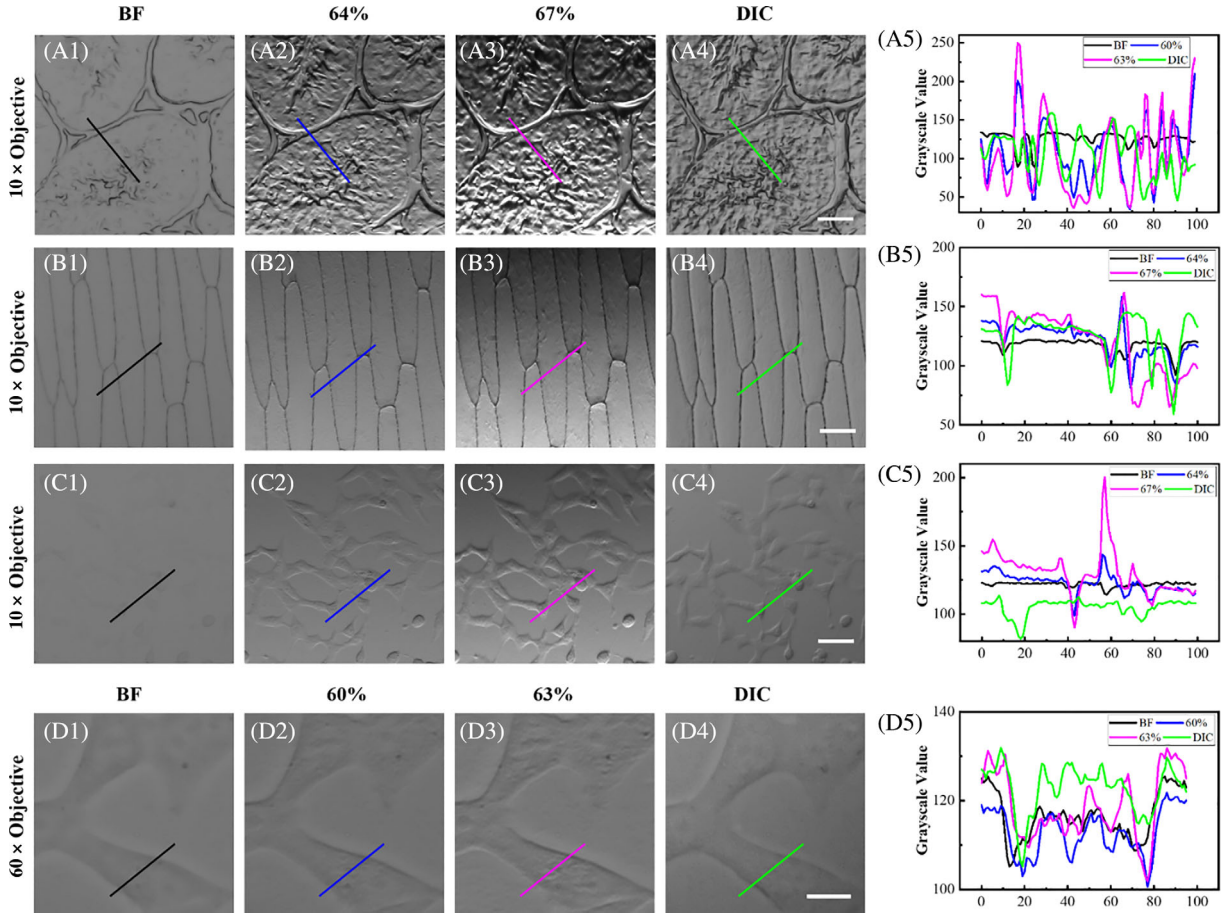

FIGURE 5 Mouse testis tissues, onion epidermic cells and HeLa cells under ×10 objective (A-C) and Hela cells under ×60 objective (D). (A1-D1) The bright field images. (A2-C2) The oblique illumination microscopy images under $R = 64\%$, (D2) $R = 60\%$. (A3-C3) $R = 67\%$ and (D3) for $R = 63\%$. (A4-D4) The differential interference contrast images. (A5-D5) The profile of gray value for mouse testis tissues, onion epidermic cells and HeLa cells. Scale bars, 50 μm (A-C) and 10 μm (D)

The other is high magnification objective including ×40 and ×60 objectives.

In the two cases of low magnification objectives, the *IQA* of HeLa cells remains stable for *R* at the range of 0% to 50%. However, the baseline for ×20 objective is much higher than ×10 objective. This means that the higher magnification objective results in higher resolution and better textures. As *R* varying from about 55% to 70%, the *IQA* curve gradually increases and appears a peak, thereafter decreases sharply. According to the peak of the *IQA* curve, the best shading ratios are 67.16% and 66.95% (red circle in the *IQA* curve), respectively, of which the corresponding images are shown in Figure 4A3,B3. When *R* reaches about 70% (green circle in the *IQA* vs *R* curve),

the sample cannot be observed due to insufficient illumination, as shown in Figure 4A4,B4. Although the initial *IQA* values are different, the best shading ratio for high imaging quality is similar according to the images captured from the ×10 and ×20 objectives.

For high magnification objectives (×40 and ×60), *IQA* vs *R* curves are shown in Figure 4C1,D1. The initial *IQA* values in these two cases are close and much larger than those in the cases of low magnification objectives. Figure 4C2,D2 show the images have no significant enhancement as the *R* increases until about 50%. When *R* is about 55% to 63%, the image quality gradually increases. The best *IQAs* in two cases are 63.74% and 62.87%, respectively. The corresponding images are shown in Figure 4C3, D3 which are better than those shown in Figure 4C2,D2, respectively. Thereafter, as *R* gradually increases, the image quality decreases. Figure 4C4,D4 show the images with the shading ratio about 75%. In these cases, the illumination is too weak to obtain effective image.

3.3 | Comparing the imaging quality of OIM and DIC

To assess oblique illumination, we compare the imaging quality of OIM and DIC. DIC, as a high-contrast method to observe unstained transparent samples, can make a relief-like three-dimensional shadow for objects. Table 1 shows the parameters of imaging quality from *IQA* of OIM and DIC with different magnification objectives. Under the ×10 objective, the largest *IQA* is 0.02435, 0.07689 and 0.02302 for onion epidermic cells, mouse testis tissues and HeLa cells, respectively. In these three cases, the best shading ratios correspond to 66.74%, 67.80% and 67.16%, respectively. This illustrates that the *IQA* for best imaging is related to specific samples, but the best shading ratios are very close. For imaging three samples under DIC microscopy, *IQA* are 0.02062, 0.04946 and 0.01464 respectively, all of which are lower than the *IQA* of the best OIM. Using *IQA* of DIC as a reference, the shading ratio for imaging quality equivalent to DIC are 63.31%, 63.52% and 60.24% for mouse testis tissues, onion epidermic cells and HeLa cells, respectively. Under the case of ×20 objective, the best shading ratio of HeLa cells is 66.95%, and the corresponding *IQA* is 0.02306. For observing HeLa cells under ×40 objective, the best ($IQA = 0.02838$) images of HeLa cells correspond to the *R* at 63.74%. In addition, the best *R* for HeLa cell under oblique illumination imaging with ×60 objective is 62.87%, and the corresponding *IQA* is 0.02625, which is better than the *IQA* (0.02015) of the counterpart DIC image. In this condition, the oblique illumination imaging with *R* of 59.13% is equivalent to the imaging quality from DIC.

Under low magnification objective, Figure 5 shows the images of onion epidermic cells, mouse testis tissues and HeLa cells, respectively. The BF images for unstained samples are shown in Figure 5A1-D1. For those images, the contrast is low. When the *R* is 64% under the ×10 objective, the *IQA* is close to that of DIC according to Table 1. For all three samples, the imaging quality from OIM with ×10 objective, as shown in Figure 5A2-C2, is very close to the corresponding images from DIC (Figure 5A4-C4). In Table 1, the image quality of DIC is lower than that of OIM with the *R* of 67% (close to largest ratio of *IQA*). Figure 5A3-C3 does indeed demonstrate the excellent imaging quality. Therefore, *R* from 64% to 67% under low magnification objective is suitable for obtaining a better contrast image. The line profiles given in Figure 5A5-C5 show that the image quality is significantly improved through OIM. The black line profiles show less fluctuations than the others because the BF image obtains less information. On the contrary, there were more fluctuations in the images with the *R* of 64% and 67%, and the line profiles from the DIC images also showed the same phenomenon. Compared with DIC imaging, OIM shows more fluctuation with R of 67% (purple curve). Compared with DIC imaging, OIM shows more fluctuation with R of 67% (purple curve). But, in this situation the image brightness is uneven, which is unfavorable for observation.

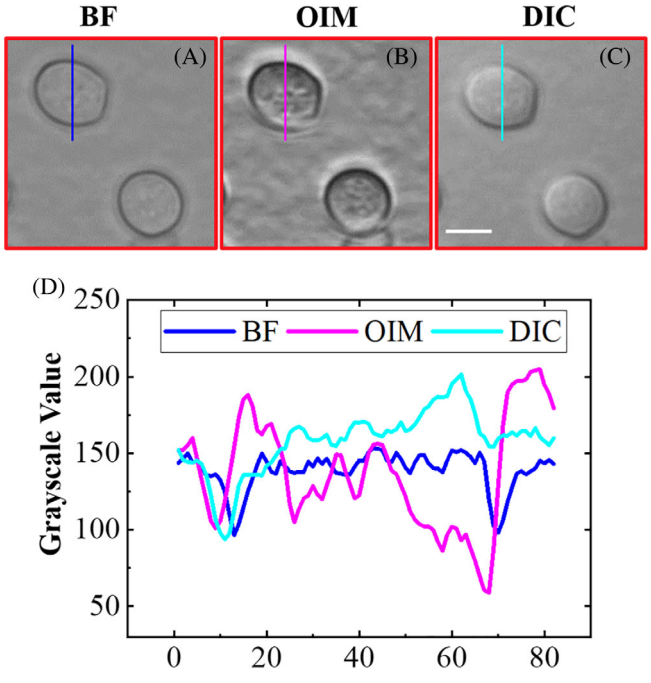

FIGURE 6 Yeast cells under ×60 objective. (A-C) Images corresponding to the red region from bright field, oblique illumination microscopy and differential interference contrast, respectively. (D) The profile of gray value for the yeast cell from (A) to (C). Scale bars, 5 μm

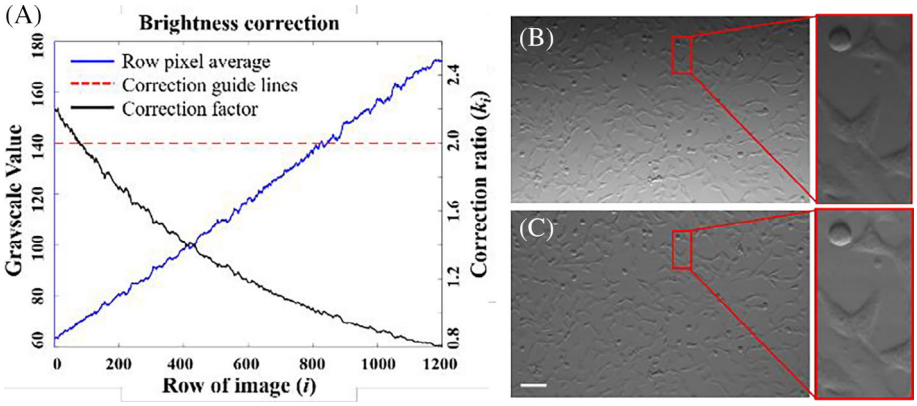

FIGURE 7 Brightness correction of imaging HeLa cells. (A) Curve of image is corrected. (B) Before correction. (C) After correction. Scale bars, 100 μm

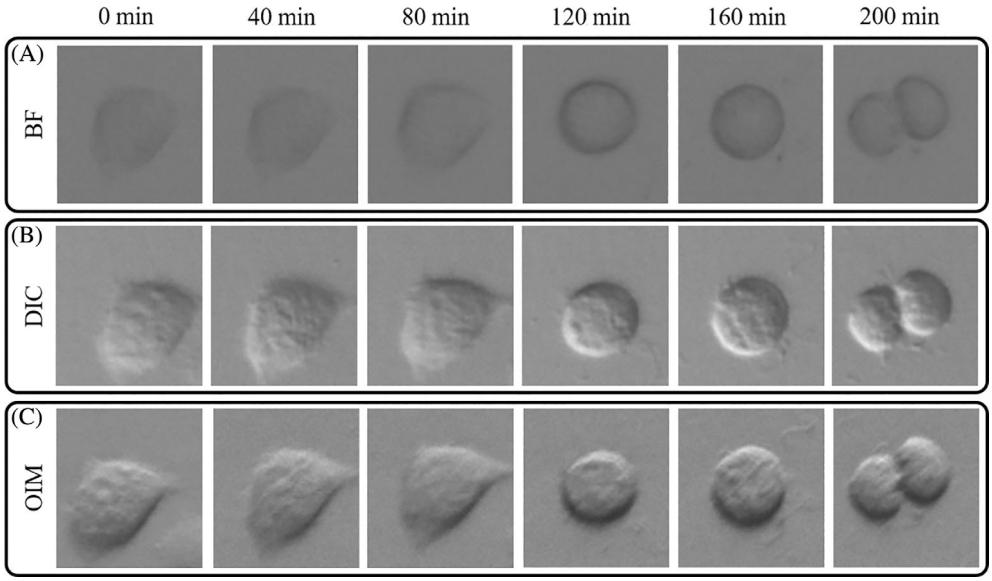

FIGURE 8 HeLa cells under three imaging modes. (A) Bright field images. (B) Differential interference contrast images. (C) Oblique illumination microscopy images. Scale bars, 20 μm

With comparison to PC microscopy (Section S4 in Supplementary Material), OIM has lower performance in mouse testis tissues (this result of image quality is similar to other studies described in Reference [28]), but has better performance in mouse testis intestines tissues.

For ×60 objective, the image of HeLa cells is shown in Figure 5D2 when the R is 60%. Obviously, it provides more detailed information than the image from BF (Figure 5D1). According to Table 1, the image quality of this sample is close to image from DIC, as shown in Figure 5D4. When R is 63% under oblique illumination, the imaging quality of Figure 5D3 is better than Figure 5D2,D4 from DIC. The line profiles in Figure 5D5 also proves this point of view. In this case, a better three-dimensional relief can be obtained. Therefore, the appropriate R for oblique illumination is 60% ~ 63% under high magnification objectives.

Under the ×60 water immersion objective, we also observed yeast cells at $R = 62\%$. The yeast cells are observed by BF microscopy, OIM and DIC, as shown in Figure 6A-C. Their *IQA* were 0.3996, 0.0497 and 0.0421, respectively. To demonstrate the difference among three imaging methods, the profile of gray value along a line on a specific cell is shown in Figure 6D. For the image from BF, the blue curve has two troughs at the edge of the cell, and the curve between the two troughs is approximately flat. It means that the detail distinction of BF image is low. When yeast cells are observed by OIM with $R = 62\%$, the purple curve between two main troughs fluctuates obviously. Compared with BF imaging, more details inside or on the surface of the yeast were observed by OIM and DIC imaging (cyan curve). A large between peaks and valleys indicates a higher image contrast. Figure 6D show that the differences between peaks and valleys in OIM profiles are even larger. Therefore, the image obtained by OIM has higher contrast.

3.4 | Brightness correction

According to Equation (8), the correction of the oblique illumination of HeLa cells is shown in Figure 7. The blue curve in Figure 7A represents the average gray value $aveI_i$

for each row of pixels. Here target gray is $Var_T = 140$ for the correction. Then the correction coefficient k_i is represented by the black curve. For OIM with the ×10 objective, the image of HeLa cells is shown in Figure 7B. The whole image appears obvious uneven brightness due to oblique illumination. On the other hand, the corrected image has uniform background brightness and good observation in field of view, as shown in Figure 7C. To demonstrate details, the images before and after correction from the same red region are shown on the right of corresponding Figure 7B,C. After correction, the imaging quality is not lower than original images for OIM (Figure S3). Thus, brightness correction can significantly improve performance for uneven brightness in OIM.

To monitor living cell with high contrast, we have integrated correction algorithm into self-programmed software with LabVIEW for image acquisition. Under OIM with ×10 objective, HeLa cells in petri dish have been recorded in bright-field and oblique-illumination at the optimal shading ratio. In our experiments, the images were acquired every 5 min within 140 min. The two imaging modes can be switched by moving out slit diaphragm quickly. Meanwhile, the images were corrected by the brightness correction algorithm. Figure 8 shows the growth status of HeLa cells under BF (A), DIC (B) and OIM (C) with optimal shading ratio at different times. These results show that the OIM method can achieve a better relief effect than DIC, and the imaging brightness is uniform. Under the optimal shading ratio for OIM, the living HeLa cells demonstrate their dynamics with high contrast (see Visualization, Video S1).

4 | DISCUSSION

In this manuscript, we construct an apparatus to assess the optimal shading ratio of the OIM, as shown in Figure 2, which consists of a sliding slit diaphragm fixed on condensers and a stepping motor that drags them. The image assessment function quantitatively assesses imaging quality and provides the best shading ratio parameter. Our results show that the shading ratio with an optimal value is between 62% and 67% under low or high magnification objectives. As shown in Figure 5, it seems that the improvement of *IQA* through optimal shading goes down with the numerical aperture. This phenomenon can be considered as a result of the depth of field going down with the numerical aperture. In oblique illumination imaging, an objective with a high depth of field will create a large interval between the zeroth-order light and the positive diffraction, which will increase the imaging contrast [29–31]. Conversely, the low depth of field with high numerical apertures makes the interval between zeroth-order light and positive diffracted smaller. This limits the ability of OIM to improve *IQA*. However, it is undeniable that the imaging contrast of OIM is still higher than that of BF, and IQA and DIC are almost identical. Evidence for this conclusion can be found in Figure 6 and Table 1. Therefore, it can be considered that the improvement of *IQA* by OIM is independent of the sample.

The data from different samples showed that the *IQA* for the tissue sample is significantly higher than the cell sample. This may be caused by the *IQA* function when collecting sample information. Currently, common IQA methods mainly extract information from images. By analyzing the quality of the image and counting the information in the sample image, the information in the final sample will be presented in numerical value. Mouse testis tissues contain more texture information than Hela cells and onion cells, so that we can see higher *IQA*.

Further, in Figures 3-5, it can be seen that the image brightness of OIM is not uniform at the low magnification objective. Especially under the optimal shading ratio, the uneven brightness of the image affects the user's observation of the sample. So, we have developed a brightness unevenness correction algorithm to form uniform background brightness for OIM, as shown in Figure 7. The correction algorithm is written in LabVIEW language, which can obtain real-time video images. The software can capture video information in real-time at the fastest frame rate of the camera. The camera we used in this paper was up to 40 fps. Of course, higher frame rate cameras can capture higher frame rate video data, and the images are obtained with uniform brightness and high contrast.

In fact, the data in the manuscript were obtained with an Olympus IX73 inverted microscope. The optimal shading ratio may vary from microscope to microscope. Our aim, however, is to modify the widely used microscope, and hopefully make this method available to more users. Users can obtain high-contrast images by following the apparatus and the methods described in this manuscript.

5 | CONCLUSION

In conclusion, we derive a method to measure the best shading ratio for oblique illumination in real microscopes. Moreover, we have deigned an apparatus on this method that, to our knowledge, is the first to provide DIC-like imaging. This apparatus does not require the insertion of complex optical components or complex calculation. Using 3D printing technology, we can

fabricate oblique illumination components (2 g of polylactic acid material, less than 0.03 dollar). Therefore, it can be used to monitor living cells in real-time with high contrast and low cost, which is expected to provide new ideas for cell analysis.

ACKNOWLEDGMENT

This work was supported by the Natural Science Foundation of Anhui Province in China under Grant 1908085MA14 and the Research Fund of Anhui Institute of Translational Medicine under Grant 2021zhyx-B16.

CONFLICT OF INTEREST

The authors declare no financial or commercial conflict of interest.

DATA AVAILABILITY STATEMENT

Data available on request from the authors.

ORCID

Tao Peng https://orcid.org/0000-0002-0120-924X
Min-Cheng Zhong https://orcid.org/0000-0002-9958-192X
Jinhua Zhou https://orcid.org/0000-0002-3704-4459

REFERENCES

[1] R. O. Wayne, *Light and Video Microscopy*, Academic Press, London, UK **2019**.
[2] F. Zernike, *Science* **1955**, *121*, 345.
[3] F. Zernike, *Physica* **1942**, *9*, 686.
[4] G. M. Nomarski, *J. Phys. Radium Paris* **1955**, *16*, 9S.
[5] R. Hoffman, L. Gross, *Appl. Opt.* **1975**, *14*, 1169.
[6] S. Bok, *Ned. Tijdschr. Geneeskd.* **1954**, *98*, 1902.
[7] E. D. Salmon, P. Tran, *Methods Cell Biol.* **2007**, *81*, 335.
[8] C. S. Guo, Y. Y. Xie, B. Sha, *Opt. Lett.* **2014**, *39*, 2338.
[9] R. Fiolka, *Opt. Express* **2016**, *24*, 29556.
[10] W. B. Piekos, *Microscopy Today* **2018**, *14*, 10.
[11] Y. Ma, S. Guo, Y. Pan, R. Fan, Z. J. Smith, S. Lane, K. Chu, *J. Biophotonics* **2019**, *12*, e201900011.
[12] Y. Han, Y. Zhang, H. Zhang, G. Han, *J. Quant. Spectrosc. Radiat. Transf.* **2009**, *110*, 1375.
[13] T. N. Ford, K. K. Chu, J. Mertz, *Nat. Methods* **2012**, *9*, 1195.
[14] V. Abbasian, Y. Ganjkhani, E. A. Akhlaghi, A. Anand, B. Javidi, A. R. Moradi, *J. Opt.* **2018**, *20*, 065301.
[15] L. Oakley, S. Zaleski, B. Males, O. Cossairt, M. Walton, *Herit. Sci.* **2020**, *8*, 27.
[16] M. Françon, *Progress in Microscopy: International Series of Monographs on Pure and Applied Biology: Modern Trends in Physiological Sciences*, Vol. 9, Elsevier, Oxford, UK **2013**.
[17] H. Schacht, *The Microscope: And Its Application to Vegetable Anatomy and Physiology*, S. Highley, London, UK **1855**.
[18] E. J. Spitta, *Microscopy: The Construction, Theory, and Use of the Microscope*, EP Dutton, Chicago, USA **1920**.
[19] T. Stephanides, *The Microscope and the Practical Principles of Observation*, Faber, London, UK **1947**.
[20] J. Ruiz-Santaquiteria, J. L. Espinosa-Aranda, O. Deniz, C. Sanchez, M. Borrego-Ramos, S. Blanco, G. Cristobal, G. Bueno, *J. Biomed. Opt.* **2018**, *23*, 1.
[21] R. Sugimoto, R. Maruyama, Y. Tamada, H. Arimoto, W. Watanabe, *Optik* **2019**, *183*, 92.
[22] W. B. Piekos, *Microsc. Res. Tech.* **1999**, *46*, 334.
[23] R. Haralick, K. Shanmugam, I. Dinstein, *IEEE Trans. Syst. Man Cybern.* **1973**, *SMC-3*, 610.
[24] C. Chen, H. Li, Y. Wei, T. Xia, Y. Tang, *IEEE Trans. Geosci. Remote Sens.* **2013**, *52*, 574.
[25] J. L. Pech Pacheco, G. Cristobal, J. Chamorro-Martinez, J. Fernandez-Valdivia, *Diatom Autofocusing in Brightfield Microscopy: A Comparative Study*, IEEE, Barcelona, Spain **2000**.
[26] K. H. Esbensen, K. H. Hjelmen, K. Kvaal, *J. Chemom.* **1996**, *10*, 569.
[27] S. Gabarda, G. Cristobal, *J. Opt. Soc. Am. A* **2008**, *24*, B42.
[28] C. Sanchez, G. Cristóbal, G. Bueno, S. Blanco, M. Borrego-Ramos, A. Olenici, J. Ruiz-Santaquiteria, *Micron* **2018**, *105*, 47.
[29] B. Kachar, *Science* **1985**, *227*, 766.
[30] S. B. Mehta, C. J. R. Sheppard, *Opt. Lett.* **2009**, *34*, 1924.
[31] R. Yi, K. K. Chu, J. Mertz, *Opt. Express* **2006**, *14*, 5191.

SUPPORTING INFORMATION

Additional supporting information can be found online in the Supporting Information section at the end of this article.

How to cite this article: M. Shao, K. Wang, Z. Wang, T. Peng, S. Zhang, J. Zhang, S. Fang, F. Wang, S. Zhang, M.-C. Zhong, Y. Wang, Z. Zhong, J. Zhou, *J. Biophotonics* **2022**, e202200122. https://doi.org/10.1002/jbio.202200122